Conformational Stability Adaptation of a Double-Stranded RNA-Binding Domain to Transfer RNA Ligand

Charles Bou-Nader, Ludovic Pecqueur, Pierre Barraud, Marc Fontecave, Carine Tisné, Sophie Sacquin-Mora, Djemel Hamdane

Conformational stability adaptation of a double-stranded RNA binding domain to transfer RNA ligand

Charles Bou-Nader[1], Ludovic Pecqueur[1], Pierre Barraud[2], Marc Fontecave[1], Carine Tisné [2], Sophie Sacquin-Mora[3], and Djemel Hamdane[1*]

[1]Laboratoire de Chimie des Processus Biologiques, CNRS-UMR 8229, Collège De France, Université Pierre et Marie Curie, 11 place Marcelin Berthelot, 75231 Paris Cedex 05, France

[2]Institut de biologie physico-chimique (IBPC), UMR 8261 CNRS/Université Paris Diderot, 13 rue Pierre et Marie Curie, Paris 75005, France.

[3]Laboratoire de Biochimie Théorique, CNRS UPR9080, Institut de Biologie Physico-Chimique, 13 rue Pierre et Marie Curie, 75005, Paris, France.

*To whom correspondence should be addressed: Djemel Hamdane, Email : djemel.hamdane@college-de-france.fr

Abbreviations: double-stranded RNA binding domain (dsRBD), human dihydrouridine synthase 2 (hDus2), double-stranded RNA (dsRNA), transfer RNA (tRNA), dihydrouridine (D), N-terminal extension (NTE), C-terminal extension (CTE), Trimethylamine N-oxide (TMAO).

Abstract

The double-stranded-RNA binding domain (dsRBD) is a broadly distributed domain among RNA-maturing enzymes. Although this domain recognizes dsRNA's structures via a conserved canonical structure adopting an α_1-$\beta_1\beta_2\beta_3$-α_2 topology, several dsRBDs can accommodate discrete structural extensions expanding further their functional repertoire. How these structural elements engage cooperative communications with the canonical structure and how they contribute to the dsRBD's overall folding are poorly understood. Here, we addressed these issues using the dsRBD of human dihydrouridine synthase-2 (hDus2) (hDus2-dsRBD) as a model. This dsRBD harbors N- and C-terminal extensions, the former being directly involved in the recognition of tRNA substrate of hDus2. These extensions engage residues that form a long-range hydrophobic network (LHN) outside the RNA-binding interface. We show by coarse-grain Brownian dynamics that the Nt-extension and its residues F359 and Y364 rigidify the major folding nucleus of the canonical structure via an indirect effect. HDus2-dsRBD unfolds following a two-state cooperative model while both F359A and Y364A mutants, designed to destabilize this LHN, unfold irreversibly. Structural and computational analyses show that these mutants are unstable due to an increase in the dynamics of the two extensions favoring solvent exposure of α2-helix and weakening the main folding nucleus rigidity. This LHN appears essential for maintaining a thermodynamic stability of the overall system and eventually a functional conformation for tRNA recognition. Altogether, our findings suggest that functional adaptability of extended dsRBDs is promoted by a cooperative hydrophobic coupling between the extensions acting as effectors and the folding nucleus of the canonical structure.

Introduction

The double-stranded RNA-binding domain (dsRBD) is a ubiquitous protein domain already present in the last universal common ancestor (*1*, *2*). This extremely versatile domain serves as a RNA, protein or RNA/protein binding module for many proteins involved in various cellular processes such as mRNA editing, genetic expression and regulation, mRNA localization and translation, ribosome assembly, stress response, cellular defense systems against foreign RNA and maturation of RNAs(*3-5*). The dsRBD folds into a conserved $\alpha_1-\beta_1\beta_2\beta_3-\alpha_2$ motif wherein two helices pack against an anti-parallel beta sheet forming a characteristic Y-shaped 3D-structure perfectly adapted to recognize the A-helix structure of dsRNAs(*2, 4, 6*). In a generally conserved mode of action, helix α1, β1-β2 loop, and helix α2 mediate interactions with the phosphodiester backbone of successive minor, major, and minor groove of the dsRNA helix (*7, 8*). Beyond this canonical topology, many dsRBDs harbor external structural extensions appended to the canonical fold, thus expanding the structural diversity of this domain (*8, 9*). Even though the role of these extensions remains largely enigmatic, some recent studies demonstrate that these additional elements could be major structural features by which dsRBD acquire new functions for the RNA or/and protein recognition(s) (*10-15*). For instance, in the dsRBD of yeast RNAse III Rnt1p, the conformational sampling of helix α3, an extension located at the C-terminus of the canonical structure and not involved in direct interaction with the RNA substrate, is important for selecting the functional conformation of canonical helix α1 that acts as a determinant of RNA stem-loop recognition by Rnt1p (*16*). We recently showed that human tRNA-dihydrouridine synthase 2 (hDus2), an enzyme responsible for synthesis of dihydrouridine (D) in tRNA's D-loop, possesses a dsRBD (hDus2-dsRBD) (*17*). Like all dihydrouridine synthases, hDus2 carries an N-terminal TIM Barrel catalytic domain (TBD) in which the redox coenzyme FMN lies in the center of the barrel and a C-terminal helical domain (HD) (Figure 1A), the latter being considered as the main tRNA binding domain of Dus enzymes (*18-21*). However, in stark contrast, we showed that, despite the presence of a HD domain, hDus2 instead use a novel extended dsRBD version flanked by a peculiar N-terminal extension (NTE) and C-terminal extension (CTE) (Figure 1A & 1B) to provide the major binding sites for tRNA substrate (*17*, *22*). In addition, we have recently shown,

through extensive structural characterization of the hDus2-dsRBD / tRNA complex, that the hDus2-dsRBD NTE is directly involved in the tRNA binding function (*15*). This is a remarkable finding since dsRBDs generally recognize basic RNA structures (A-helix and stem-loop) whereas tRNAs adopt a more complex L-shaped architecture involving tertiary interactions. Moreover, it is the first example of an extension involved in direct interaction with the RNA substrate. While hDus2-dsRBD retains a conventional dsRNA recognition capability, the NTE provides additional residues, Q367, R361 and R362 involved in the recognition of the peculiar tertiary structure of the tRNA(*15*). Curiously, when examining tRNA binding at the single residue level by NMR spectroscopy, we observe that in addition to the expected canonical interactions, the formation of a dsRBD/tRNA complex produces major resonance shifts in some residues of the NTE not involved in tRNA binding(*15*). Even more surprising was the fact that several residues of the CTE are also affected, even though they are located far from the RNA binding interface. These effects suggest a strong dynamical correlation between the canonical structure of the dsRBD and its extensions. More generally, these findings imply that cooperative communications between these extensions and the canonical structure exist and they may be important for connecting efficiently the function to the overall protein folding. How these structural elements engage cooperative communications with the canonical structure and how they contribute to the dsRBD's overall folding are fundamental issues since conformational dynamic and flexibility of proteins are well known to drive biological functions (*23*-*25*). By combining computational, biophysical and structural analysis we address the molecular mechanism by which the extensions engage cooperative communications with the canonical structure to adapt the folding and the functional conformation of hDus2-dsRBD to tRNA recognition and provide evidences that this cooperativity is governed by hydrophobic interactions.

Materials and Methods

Protein and tRNA purification

Wild type dsRBD of human dihydrouridine synthase 2 was cloned in a pET11d vector between BamHI and NcoI and expressed in BL21(DE3) (Novagen) in LB medium as previously described(*17*).

Point mutations were carried out with Q5® Site-directed mutagenesis kit (New England BioLabs) following the recommended procedure and done on dsRDB-pET11d vector. The resulting mutants were purified with the same procedure as used for the wild type protein except for ΔNTE mutant that was induced at $O.D._{600}$ 0.6 and left overnight at 16°C. For NMR experiments, cells containing the plasmid encoding dsRDB were grown in M9 minimal medium supplemented with 1 g/L of $^{15}NH_4Cl$ for ^{15}N-labeling or 1 g/L $^{15}NH_4Cl$ and 2 g/L ^{13}C-glucose for $^{13}C/^{15}N$-labeling. The labelled proteins were purified following the protocol used for unlabeled dsRDB. *Homo sapiens* $tRNA^{Lys}_3$ was expressed in *E. coli* (JM101TR strain) from a recombinant plasmid and purified as previously described(*26*).

tRNA binding assays

Electrophoretic mobility shift assays were carried for wild-type dsRBD and its different mutants using a 6 % native (19:1) PAGE at 4 °C with 100 V. Increased concentrations of proteins were added to a fix concentration of *Homo sapiens* $tRNA^{Lys}_3$ (1µM) and incubated at room temperature for 20 minutes in 50 mM Tris-HCl pH 8, 10 % glycerol, 5 mM DTT and 150 mM ammonium acetate prior to migration. RNA was visualized by toluidine coloration and quantified using ImageJ (https://imagej.nih.gov/ij/index.html).

Crystallization, data collection, structure determination and refinement

F359A dsRBD mutant crystallized in 2 M ammonium sulfate, 50 mM sodium cacodylate pH 6 and 15 mM magnesium acetate. Crystals were obtained after 3 days and were cryoprotected using 15 % glycerol before flash freezing. The structure was phased by molecular replacement using PDB 4wft as initial model in phaser and refined with Phenix(*27*). All diffraction data collections were carried out on single crystals at the micro focused PROXIMA-2 beamline at the SOLEIL synchrotron (Saint-Aubin, France) at 100 K using an ADSC Quantum 315r detector for the protein-RNA structure and an Eiger X-9M for both mutants with a wavelength of 0.9801 Å. Data were indexed, processed, merged and scaled using XDS or autoPROC(*28*).

NMR experiments

NMR spectra measurements and backbone resonance assignment of wild type hDus2-dsRBD (residues 337-450) were previously reported (*15*). For F359A and Y364A dsRBD mutants, the NMR spectra were recorded at 298 K on a Bruker Avance III HD 700 MHz in a buffer containing 25 mM sodium phosphate pH 6.5, 20 mM sodium chloride, 1 mM dithiothreitol (DTT) and 10 % (v/v) D_2O. The data were processed using TOPSPIN 3.5 (Bruker) and analyzed with Sparky (www.cgl.ucsf.edu/home/sparky/). Backbone resonance assignments for F359A and Y364A dsRBD mutants were performed with 2D (^{1}H,^{15}N)-HSQC, 3D HNCA, 3D CBCA(CO)NH, 3D HNCO and 3D NOESY-(^{1}H,^{15}N)-HSQC.

SAXS data collection, analysis and model generation

SAXS experiments were performed at the SWING beamline at the SOLEIL synchrotron (Saint-Aubin, France) using an online high-performance liquid chromatography (HPLC). All scattering intensities were collected on the elution peaks after injection on a BioSEC-3 column (Agilent) equilibrated in 25 mM Tris-HCl pH 8, 100 mM NaCl, 1 mM $MgCl_2$ and 5 % glycerol to reduce radiation damage. Data were processed using FOXTROT (https://www.synchrotron-soleil.fr/fr/lignes-de-lumiere/swing). The radius of gyration (R_g) was calculated by the Guinier approximation.

Circular dichroism

Circular dichroism spectra were recorded on a Chirascan™-plus CD Spectrometer (Applied Photophysics). The far ultraviolet spectra (200–260 nm) were measured at 20°C in quartz cells of 0.4 cm optical path length. The final concentration of dsRBD proteins was 5 µM in 25 mM sodium phosphate pH 8. Spectra were acquired at a resolution of 1 nm, with time per points set at 0.7 second and a bandwidth of 1 nm. All spectra were corrected from the contribution of the buffer and are an average of seven accumulations.

Fluorescence

All fluorescence emission spectra were recorded in a 4/10 mm quartz cuvette at 20°C in a Cary eclipse fluorescence spectrophotometer (Varian). The fluorescence of wild type and mutants hDus2-dsRBD were recorded at λ_{ex} = 295 nm between 305-500 nm using a slit width of excitation and emission at 5/5

mm, respectively. The fluorescence was measured at various protein concentrations (5, 10, 20, 40 and 80 µM in 50 mM sodium phosphate pH 8 (with or without 1 M TMAO). In urea-induced denaturation equilibrium, all the proteins were at 5 µM. Before recording the spectra, protein and urea were incubated for 1 hour at 20°C to reach equilibrium. The thermodynamic parameters characterizing the stability of wild type hDus2-dsRDB were determined by fitting maximum fluorescence intensity wavelength (λ_{max}) to a two-states model (N ⇔ D) equation based on the linear relationship between Gibbs energy and concentration of denaturant: $\Delta G = \Delta G° - m[urea]$, where $\Delta G°$ is the free energy for converting the native to the unfolded state at zero urea and m an empirical constant corresponding to the slope of plot of ΔG against [*urea*]. Cm is the urea concentration required to denature half of the dsRBD molecules. Urea-denaturation curves were fitted to the following two-state equation: $\lambda(\text{urea}) = (\lambda N + \lambda D * \exp(-(\Delta G° - m[urea])/RT)) / (1+\exp(-(\Delta G° - m[urea])/RT)$, where λN and λD are the maximum fluorescence intensity wavelength of the native and denatured states, respectively.

Stopped-flow kinetics

The fast kinetic of urea-induced dsRBD denaturation were performed on a TGK Scientific SF-61DX2 stopped-flow fluorescence spectrophotometer equipped with a temperature-controlled circulating water bath. Protein (5 µM) was rapidly mixed with an equal volume of urea. All reactions were performed at 20°C in 50 mM sodium phosphate pH 8.0. The kinetics were followed by recording protein fluorescence after exciting at 295 nm. Up to five transients were collected and averaged for each condition. Background signal was determined against buffer to allow data scaling. The observed rate (k_u) was determined by fitting the averaged transient to a single exponential equation $F(t) = F0 + A(1-\exp(-k_u * t))$. k_u^{H2O} and $m_u^{\#}$ were determined from fitting the data ln ku versus urea by the following equation: $\ln k_u = \ln k_u^{H2O} + m_u^{\#}[\text{urea}]$. All the fittings were performed using SigmaPlot 12 software.

Mild trypsinolysis and MALDI-MS analysis

Mild trypsinolysis was carried at room temperature in 50 mM Tris-HCl pH 8 and 150 mM NaCl in a final volume of 20 µL. 15 µg of proteins (dsRBD or F359A or Y364A mutants) was added and incubated with 1/200 ratio of trypsin. The proteolysis reaction was quenched by adding 2 mM of PMSF and heated in loading buffer for 1 min at 90 °C. When in the presence of 3 molar equivalent tRNA, the mixture was incubated for 20 minutes at room temperature prior to addition of 1/100 ratio of trypsin. Samples were loaded on a 18 % SDS-polyacrylamid gel and analyzed by coomassie blue staining. The excised bands were enzymatically digested by adding trypsin or Glu-C (Promega) and incubated overnight at room temperature. Peptides were extracted in 60 % acetonitrile and 0.1 % v/v formic acid and mixed with α-cyano-4-hydroxycinnamic acid (10 mg/ml, 50% CH_3CN; Sigma-Aldrich); for better identification of N termini, chemical labeling with succinimidyloxycarbonylmethyl tri-(2,4,6-trimethoxyphenyl) phosphonium (TMPP-Ac-OSu; Sigma Aldrich) was performed. Crystals were analyzed by MALDI-TOF-TOF 5800 (ABSciex). Peak lists were processed and analyzed with ProteinPilot software (ABSciex) using the MASCOT algorithm. The search parameters were as follows: hDus2-dsRBD sequence; digest reagent Glu-C or trypsin; fixed modification, carbamidomethylation of cysteines; possible modification, oxidation of methionines.

Coarse-grain simulations

Coarse-Grain Brownian Dynamics simulations were performed using the ProPHet program(*29-31*) (http://bioserv.rpbs.univ-paris-diderot.fr/services/ProPHet/) on the crystallographic structure of hDus2-dsRBD (pdb code 4WFT)(*17*), with and without its N-terminal extension, and seven additional dsRBD domains (from pdb files 1DI2(*7*), 3ADG(*32*), 2MDR(*13*), 1T4O(*10*), 2CPN, 2LJH(*33*) and 2NUG(*34*)). The simulations use a reduced protein model, where each amino acid is represented by one pseudo-atom located at the C_α position, and either one or two (for larger residues) pseudo-atoms replacing the side chain (with the exception of Gly)(*35*). Interactions between the pseudo-atoms are treated according to the standard elastic network model (*36*). The elastic network model is a simplification of the heterogeneity of internal protein forces, as all pseudo-atoms lying closer than 9 Å are joined with quadratic springs having a force constant of 0.6 kcal mol^{-1} $Å^{-2}$. Springs are assumed to be relaxed in the starting conformation of the protein. The simulations use an implicit solvent

representation via the diffusion and random displacement terms in the equation of motion(*37*), and hydrodynamic interactions are included through the diffusion tensor(*38*). The Brownian dynamics simulations have been performed with 200,000 steps at an interval of 10 fs and at a temperature of 300 K. Effective force constants for displacing each particle i are then calculated as

$$k_i = \frac{3k_B T}{\left\langle \left(d_i - \langle d_i \rangle\right)^2 \right\rangle},$$

where the brackets indicate the average taken over the whole simulation, k_B is the Boltzmann constant, and d_i is the average distance of particle *i* from the other particles *j* in the protein, excluding the pseudoatoms that belong to the same residue *m* as particle *i*. The distances between the C_α pseudoatom of residue m and the C_α pseudoatoms of the adjacent residues *m + 1* and *m – 1* are not included in the average. The force constant associated with each residue *m* is taken to be the average of the force constants calculated according to equation 1 for each of the pseudoatoms *i* forming the residue. Within this framework, the mechanical properties of a protein are described at the residue level by its "rigidity profile", that is, by the ordered sequence of the force constants (in kcal mol^{-1} $Å^{-2}$) calculated for each residue.

Finally, for each protein, we define *rigid residues* as the residues presenting a force constant k_i

$$k_i \geq \langle k \rangle_P + \sigma(k)_P$$

which satisfies the following criterion :

$\langle k \rangle_P$ being the residues force constant mean value for the whole protein (or a single domain in case of multi-domain proteins) and $\sigma(k)_P$ its variance.

Sequence alignments

All sequences for the dsRBD domains were aligned using the online COBALT (*39*) tool (http://www.st-va.ncbi.nlm.nih.gov/tools/cobalt/cobalt.cgi?CMD=Web) with the defaults parameters. Rigid residues that were identified using the definition given in the previous section are highlighted in bold and color along the protein sequences in Figure S1.

All-atom Classical Molecular Dynamics simulations

For the wild type and F359A mutant of hDus2-dsRBD, we performed all-atom, classical Molecular Dynamics (MD) simulations. We used Gromacs, version 5.0.4, with the OPLS-AA forcefield (*40*) with periodic boundary conditions. The first step of the simulation procedure is an *in vacuo* minimization of the structure with the steepest descent algorithm during 1000 steps without any constraints. We added a triclinic water box of 2 nm around the protein, filled with TIP3P molecule type (*41*) and the system was neutralized with the addition of ions randomly placed in the box while maintaining the NaCl concentration at 150 mM. The whole system contains around 1 500 atoms, 15 000 water molecules and 90 ions (with approximatively 42 Na^+ and 47 Cl^-). A second minimization step was performed with the same set of parameters than before during 5000 steps to prevent possible water clashes with the protein. Molecular dynamics were carried out using an integration time step of 2 fs. Initial heating and pre-equilibration were carried out by assigning random velocities from the Maxwell-Boltzmann distribution followed by 100 ps of dynamics under NVT conditions, then 100 ps under NPT conditions. During this process and for all subsequent dynamics the temperature was fixed at 300 K using the velocity rescale method (*42*). All bonds were constrained with the LINCS algorithm (*43*) and electrostatic interactions were computed using the Particle Mesh Ewald method[(44)]. For the pressure coupling during the NPT equilibration, we used the Parinello-Rahman method(*45*) at the value of 1 atm. Production phases were finally done using the same set of parameters and algorithms during 200 ns. Trajectories were saved every 10 ps.

Results

Identification of a hydrophobic network potentially involved in cooperative communications between the canonical structure and its extensions

To determine the molecular origin behind these cooperative communications, we carefully examined potential interactions between the NTE and the canonical $\alpha_1-\beta_1\beta_2\beta_3-\alpha_2$ fold. NTE passes above the middle of helix α2 and forms in *trans* a 3_{-10} helix turn, containing the R361-R362 residues, followed by a loop structured into a stiff U-turn containing Q367, and then finishes near the CTE (Figure 1A).

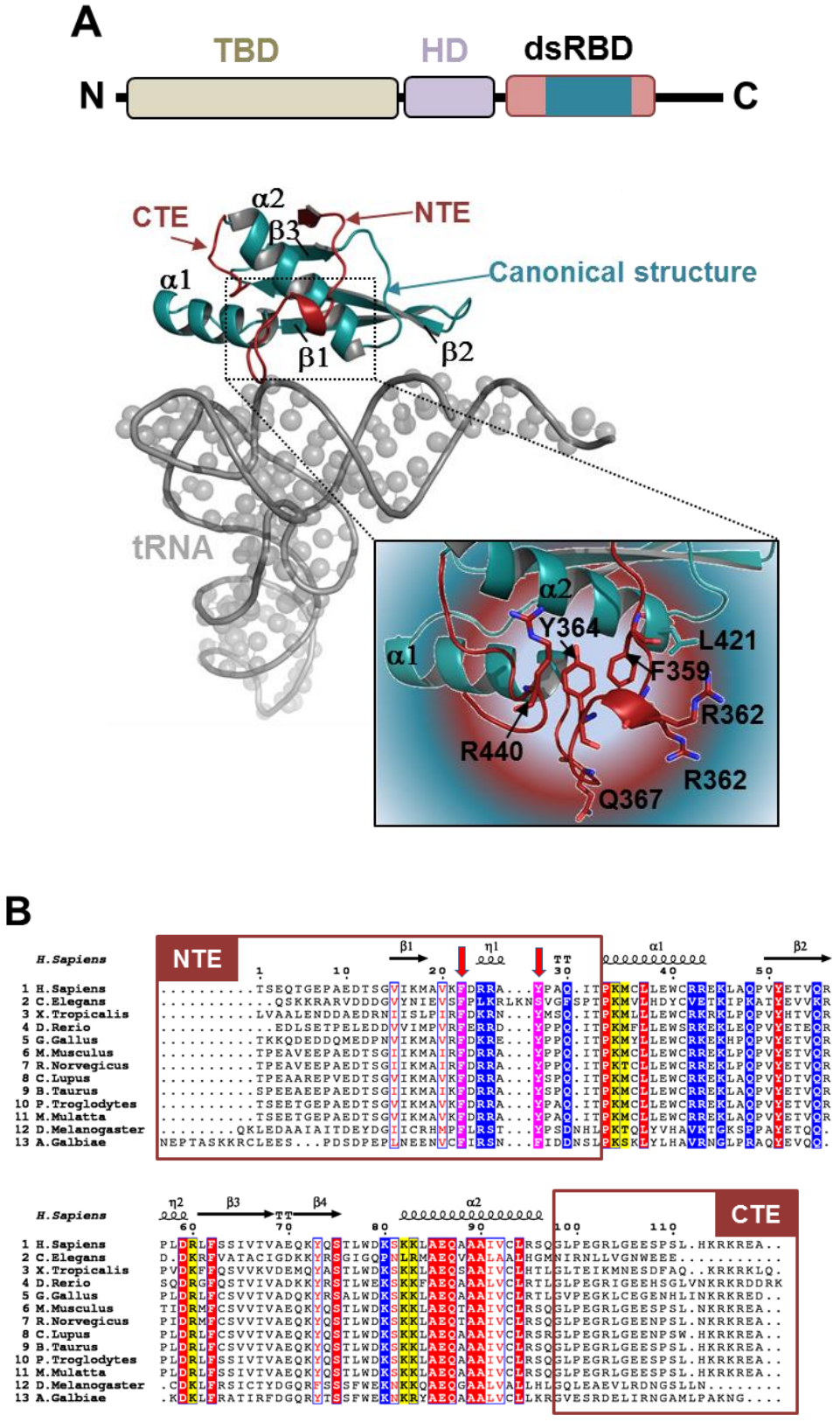

Figure 1 Structural organization of hDus2-dsRBD. (A) On top is shown the domain modularity of hDus2, which is likely conserved among animal Dus2. In wheat is the Tim Barrel domain (TBD), which carries the FMN cofactor required for the reduction of U20 into D20 in the tRNA, the helical domain (HD) is in purple and serves as the major tRNA binding module in other dihydrouridine synthase paralogues. The canonical fold of the dsRBD is in turquoise while the NTE and CTE are in

pink. In the middle is represented the structural model of hDus2-dsRBD/tRNA complex as published previously (15). Refer to (15) for more details on how this model was built. The tRNA is represented in gray. Bottom, zoom on the NTE and CTE regions. **(B)** Amino-acid sequence alignment of dsRBDs from animal Dus2 enzymes. In yellow are shown conserved residues across class A dsRBDs involved in RNA contacts. In red are residues involved in folding. In blue are residues implicated in RNA recognition solely conserved in Dus2 type dsRBDs. In magenta are shown the two conserved residues identified in this study as important for proper folding and stability of these dsRBDs. β1 strand and η1 3-10 helix belong to the NTE whereas β2, β3, β4 and α1, α2 are the secondary structures of the canonical structure of hDus2-dsRBD. The boundaries of the CTE and NTE are contained within the brown boxes. The red arrows inside the NTE box indicate the position of F359 and Y364.

This peculiar geometrical structure creates an insulating hydrophobic pocket delimitated by the NTE itself, the external face of helix α2 and the CTE. Inside this pocket, hydrophobic interactions aligned over a 15 Å straight vector formed by L421-F359-Y364-R440 appear to cooperate to tighten both ends of helix α2 (Figure 1A). In that respect, our previous NMR study picked up indirect implication of F359 and Y364 in tRNA binding (*15*). Analysis of sequence alignment reveals that these residues are conserved among the dsRBD of animal's Dus2 (Figure 1B). Therefore, these hydrophobic residues could be important to properly orient the NTE relative to the canonical dsRBD domain, in order to present R361-R362-Q367 in a competent configuration for specific tRNA binding.

Influence of the NTE, F359 and Y364 on the mechanical landscape of hDus2-dsRBD

To test this hypothesis, we used a computational approach relying on coarse-grain Brownian dynamics to characterize the mechanical landscape of hDus2-dsRBD. This type of approach has been successfully applied to determine the rigidity profiles of various proteins and to specifically identify rigid residues constituting their folding nucleus (*46, 47*). From the rigidity profiles calculated on seven dsRBDs from different organisms (Figure S1), and following the protocol detailed in reference (46), we define the folding nucleus in the dsRDB fold as the subset of conserved positions along the protein sequences that present rigidity peaks in most of the rigidity profiles of the structures under study. This approach leads to the identification of a well-defined folding nucleus, which comprises six residues. In hDus2-dsRBD, this folding nucleus corresponds to S401 and V403 in the β2 strand, and E423, A426, A427 and C430 in helix α2 (Figure 2A).

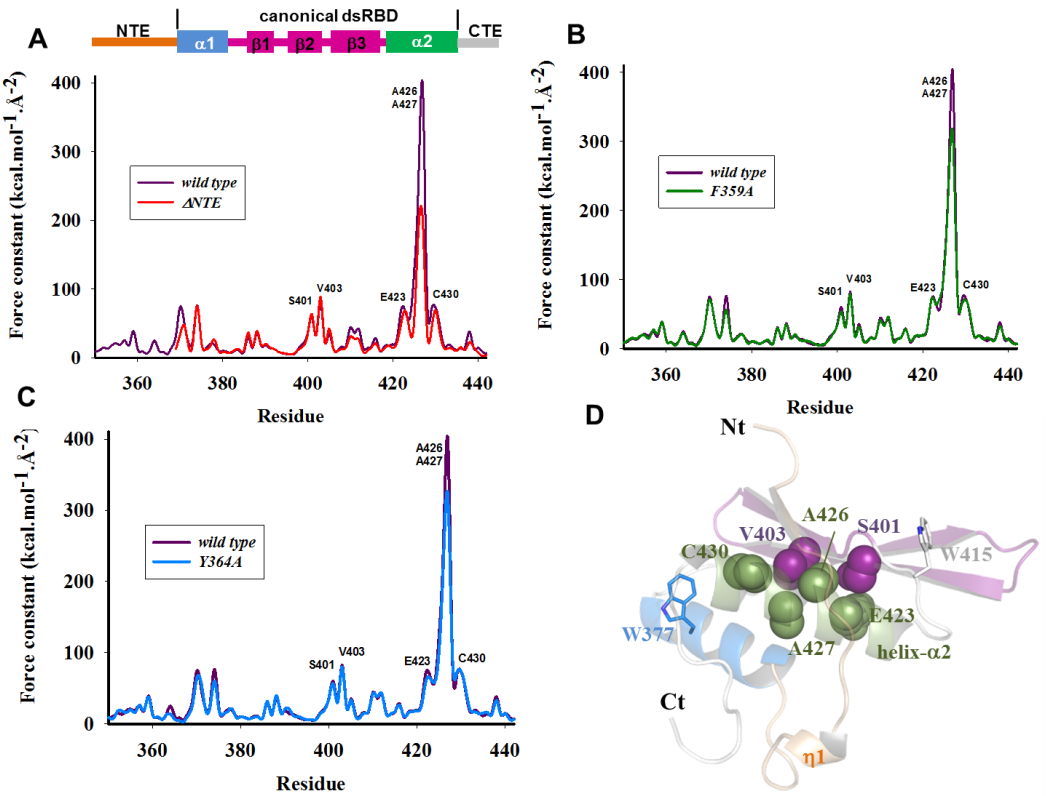

Figure 2 Role of the NTE on the mechanical landscape of hDus2-dsRBD. (**A), (B) and (C)** Rigidity profiles obtained from coarse-grain Brownian dynamics simulations for wild type dsRBD (violet), ΔNTE variant form (red), F359A (green) and Y364A (green) mutants, respectively. The force constants are in kcal mol^{-1} $Å^{-2}$. Residues are placed following the secondary structure of human dsRBD as represented schematically on top of the graph. **(D)** Cartoon representation of hDus2-dsRBD crystal structure showing the residues forming the folding nucleus as determined from **(A)**.

The position of these residues on the 3D-structure of hDus2-dsRBD is shown in Figure 2D. The mechanical properties of these residues are qualitatively similar for all dsRDBs as expected for proteins sharing the same fold (*48*) (Figure S1). However, in hDus2-dsRBD, the force constant corresponding to the A426 and A427 rigidity peak, reaching roughly 400 kcal mol^{-1} $Å^{-2}$, is much higher than in others dsRBDs (for example it reaches 160 kcal mol^{-1} $Å^{-2}$ in dsRBD from *X. laevis* RBPA protein).

Remarkably, when reproducing the calculations with a shorter version of hDus2-dsRBD lacking the NTE (ΔNTE), we observe that the resulting rigidity profile is globally unaffected, except for the peak corresponding to A426-A427, where the associated constant drops down significantly to ~ 200 kcal mol^{-1} $Å^{-2}$ as compared to the full length counterpart (Figure 2A). Similarly, replacement of F359 or

Y364 by an alanine decreases the rigidity associated to A426-A427 to ~ 309 and 320 kcal mol^{-1} $Å^{-2}$, respectively (Figure 2B & 2C). A426-A427 are located on the internal face of helix α2 and are not in direct contact with residues from the NTE (Figure 2D). Hence our computational characterization of hDus2-dsRBD indicates that the alanine pair A426-A427 is an important element the NTE and its residues F359 and Y364.

ΔNTE, F359A and Y364A destabilize the secondary and tertiary structures of hDus2-dsRBD

To further assess the impact of the NTE on hDus2-dsRBD, we generated a ΔNTE deletion, and two single point F359A and Y364A mutants and characterized first their ability to bind tRNA and then their structural properties. As shown by gel shift assay, the wild type dsRBD forms a stable complex with human $tRNA^{Lys}_3$ (observed K_D ~ 4 μM), while the ΔNTE mutant does not bind tRNA (Figure 3). In contrast, the two single variants retain tRNA binding with a reduced affinity (2.6 and 1.2-fold for F359A and Y346A, respectively) (Figure 3). Characterization of the secondary structures by circular dichroism revealed a significant reduction of alpha helix content (~ 40 %), converted to random coil, in the ΔNTE variant compared to the wild type dsRBD (Figure 4A).

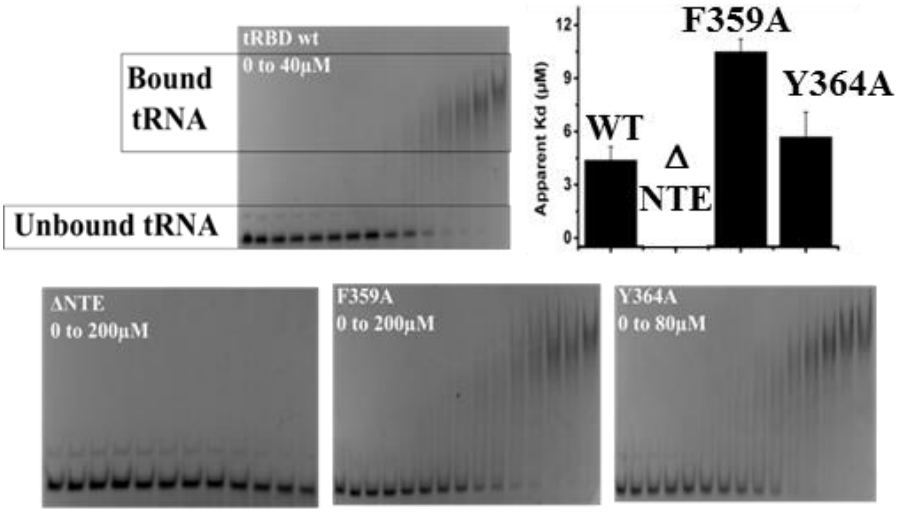

Figure 3 Electrophoretic mobility shift assay experiments measuring affinities of wild type hDus2-dsRBD and its mutants for tRNA. Gel shift for the wild-type and mutants dsRDB are shown in the top and bottom, respectively. The bands corresponding to free and dsRDB bound tRNA are black boxed. In all cases, 1 μM of $tRNA^{Lys3}$ was used while the range of protein concentration is

indicated in each case. The histogram shows apparent Kd in µM of wild type, ΔNTE, F359A or Y364A dsRDB for $tRNA^{Lys3}$.

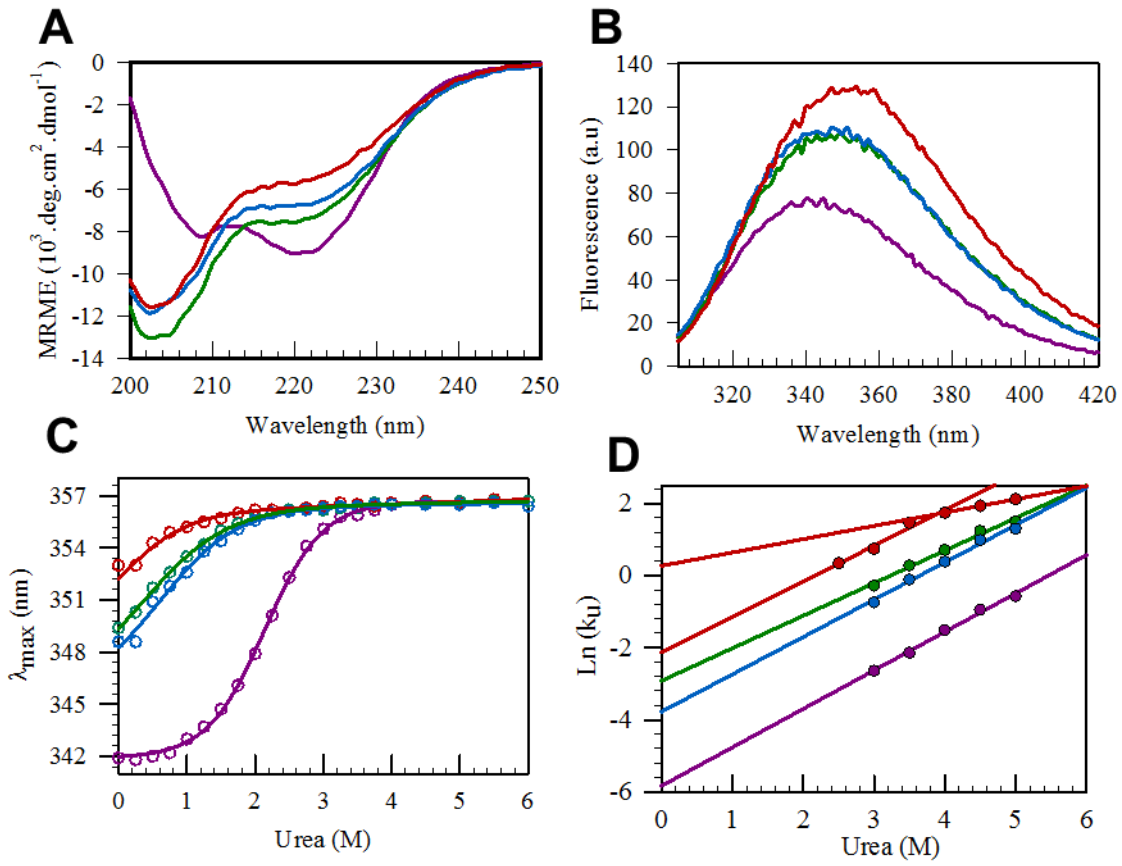

Figure 4 Biophysical characterization of the folding and stability of wild type hDus2-dsRBD and its NTE mutants. (A), far-UV circular dichroism spectrum of wild type dsRBD (violet), ΔNTE (red), F359A (green) and Y364A (blue) mutants. **(B)** protein fluorescence emission spectrum at an excitation of 295 nm, which is specific to tryptophan residues, of wild type dsRBD (violet), ΔNTE (red), F359A (green) and Y364A (blue) mutants. **(C)** urea-induced equilibrium denaturation curves followed by protein fluorescence for wild type dsRBD (violet), ΔNTE (red), F359A (green) and Y364A (blue) mutants. **(D)** Denaturation dependence of the natural logarithm of the observed rate constants for unfolding of wild type (violet), ΔNTE (red), F359A (green) and Y364A (blue) hDus2-dsRBD on the concentration of urea.

The tertiary structure was also probed by recording intrinsic tryptophan fluorescence of the proteins. hDus2-dsRBD contains two tryptophan residues, W377 located at the C-terminus of helix α1 facing the CTE and W415 located in the loop between sheet β3 and helix α2 (Figure 2D). The maximum fluorescence (λ_{max}) in the wild type dsRBD of 342 nm indicates that both tryptophans are in a hydrophobic environment. Conversely, deleting the NTE enhances the fluorescence by ~ 40 % and induces a huge 10-nm red shift of λ_{max} indicating that the tryptophan residues are in a more polar

environment (Figure 4B). Interestingly, circular dichroism and tryptophan fluorescence studies revealed that both F359A and Y364 mutants carry secondary and tertiary structures that are intermediates between those of the wild type and ΔNTE dsRBDs (Figure 4A & 4B). It should be mentioned that a complete exposure of tryptophan residues to the solvent, obtained after full denaturation of the wild type or the dsRBD mutants in 6 M urea, leads to a λ_{max} ~ 357 nm. Hence the deletion of NTE or mutation of F359 or Y364 dramatically disrupts both the tertiary and secondary structures of hDus2-dsRBD leading to a partially unfolded protein.

NTE, F359 and Y364 are important for the thermodynamic stability of hDus2-dsRBD

We then investigated the overall stability of wild type dsRBD and its NTE mutants by urea-induced denaturation experiments. Urea-induced denaturation equilibrium experiments indicate that the dsRBD of hDus2 unfolds cooperatively following a reversible two-state model with a ΔG^0 ~ 3.3 +/- 0.2 kcal.mol^{-1} and an m-value ~ 1.5 +/- 0.1 kcal.mol^{-1}.M^{-1} (Figure 4C & Table S1). However, in the case of ΔNTE, F359A and Y364A variants, the protein unfolds irreversibly suggesting that the folding cooperativity characterizing hDus2-dsRBD is lost likely due to a missing driving force (Figure 4C). This makes the determination of the thermodynamic constants useless for these mutants. Alternatively, the destabilizing effect induced by the deletion and single mutations can be quantitatively assessed from the stopped-flow unfolding kinetics performed at various urea concentrations allowing determination of the unfolding rate constant in water (k_u^{H2O}) extrapolated from the free-energy linear dependence with urea concentration. For the wild type dsRBD, this approach leads to a low k_u^{H2O} ~ 3.10^{-3} s^{-1} value associated with a gradient $m^{\#}_u$ ~ 0.6 kcal.mol^{-1}.M^{-1} (proportional to the change in surface area exposed to the solvent between the native and the transition state (TS)) (Figure 4D & Table S1). For ΔNTE mutant, the behavior is more complex as revealed by two transitions suggesting a change in the rate limiting step at urea concentrations above 1.5 M probably due to an additional TS. The first transition is characterized by a k_u^{H2O} 40 times faster than that of the wild type dsRBD with a similar $m^{\#}_u$ while the second transition is 433 times faster than the wild type and seems to involve a more compact TS2 as indicated by the lower $m^{\#}_u$ value. As judged from their k_u^{H2O}, the single mutants

are more stable than ΔNTE mutant but less stable than the wild type dsRBD by a factor of ~ 18 and 8 for F359A and Y364A, respectively (Figure 4D & Table S1). In contrast, their $m^{\#}_{u}$ values do not significantly change compared to the wild-type protein suggesting that the destabilization of the dsRBD structure occurs at the ground state level. Altogether, in agreement with the coarse-grain simulations, the NTE is essential to the thermodynamic stability of hDus2-dsRBD and its deletion or mutation of F359 or Y364 leads to a kinetically unstable protein.

The hydrophobic residues, F359 and Y364, of NTE promote dsRBD protein matrix compactness

The conformational stability of intrinsically unstable proteins are extremely sensitive to environmental conditions such as osmolytes, crowding agents or protein concentrations, which stabilize directly the native state by the physical principle of exclusion volume(*49-51*). We tested whether the matrix packing of F359A and Y364A mutants depends on the protein concentration or the presence of osmolytes in the media by following their effect on the fluorescence λ_{max}.

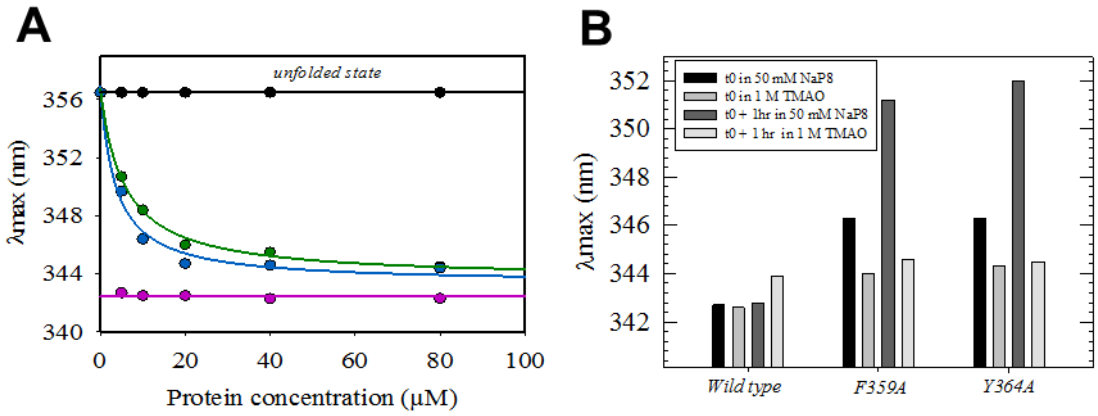

Figure 5 Effect of the protein concentration and osmolyte on the tertiary structure of the wild type dsRBD and its NTE mutants. (A) Effect of final protein concentration on the tryptophan's fluorescence of wild type folded (pink) and fully unfolded by 6 M urea (black) dsRDB, F359A (green) and Y364A (blue) mutants. **(B)** Effect of 1 M TMAO on tryptophan's fluorescence of wild type dsRDB, F359A and Y364A dsRDB mutants.

As anticipated, we observed that λ_{max} of both mutants decrease with the final protein concentration or in the presence of 1 M TMAO, which is a natural osmolyte (Figure 5A & 5B). In contrast, neither the protein concentration nor TMAO have a significant effect on the wild type dsRBD. Furthermore, TMAO strongly stabilizes the mutants even after 1 hour incubation (Figure 5B). Altogether, these

results suggest that mutation of F359 and Y364 lead to a loosely packed dsRBD. These residues of the NTE ensure a thermodynamic stability for the overall dsRBD by stabilizing the matrix compactness of the canonical structure.

F359 and Y364 promote cooperative communications between the NTE, CTE and the canonical domain for a functional dsRBD conformation

Although unstable proteins make determination of their structure by X-ray crystallography a challenge, we anticipated that the high protein density required to crystallize these unstable dsRBDs could stabilize a conformational state that is otherwise elusive. It was therefore essential to obtain such a structure to understand how this hydrophobic network functions on the molecular level and, eventually, why its absence provokes folding issues within the canonical structure. This strategy proved to be successful with the F359A variant, as we crystallized and solved its structure with a 2.2 Å resolution (Figure 6 & Table S2).

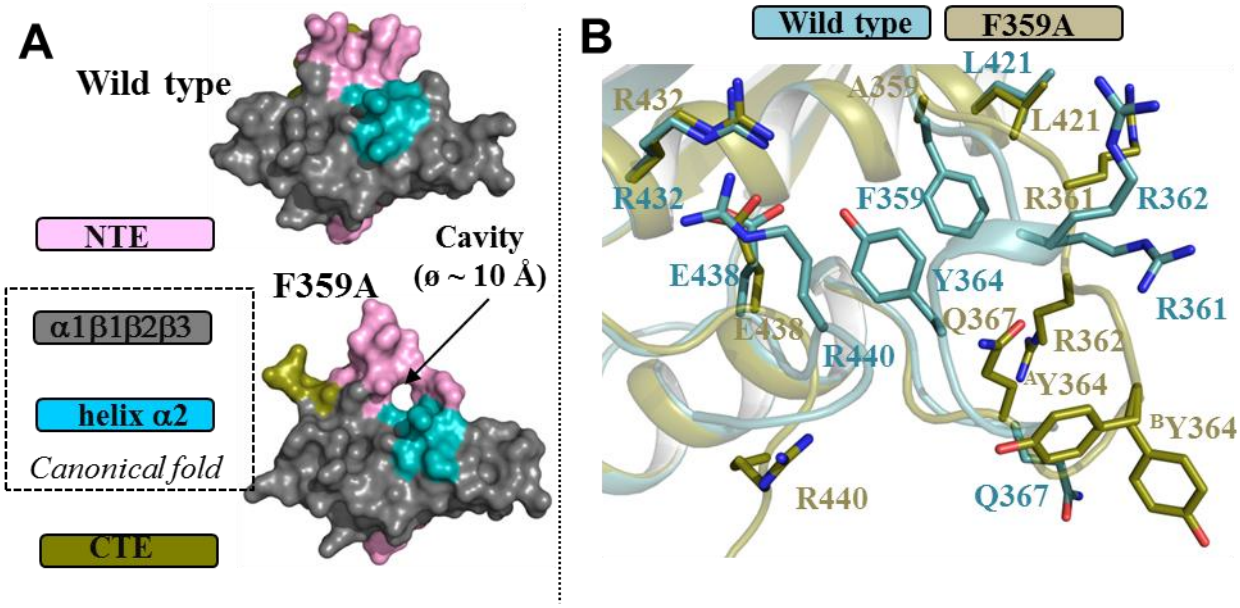

Figure 6 Structural evidence for a cooperative hydrophobic network in maintaining functional conformation. (A) Structures of wild type (top) and F359A dsRBD (bottom) represented in a surface mode. The arrow indicates the position of the large solvent accessible cavity resulting from F359A mutation. **(B)** Structural alignment between wild type and F359A dsRBDs showing the perturbation induced by the mutation in the NTE and CTE regions. The structure of the wild type is in cyan while that of F359A dsRBD (deep olive). The change in distance between the specified atom of a given residue in the wild type and in the F359A mutant are as follow: R361(Cζ-Cζ) ~ 9.6 Å; R362(Cζ-Cζ) ~ 15.5 Å); Y364(Cβ-Cβ) ~ 9 Å; R440(Cβ-Cβ) ~ 8 Å.

Remarkably, this structure reveals that the helix α1 and the β-sheet remain unchanged while significant conformational alterations are observed in the NTE, CTE and around helix α2 (Figure S2A). The hydrophobic pocket generated by the latter is disrupted leading to the formation of a large solvent accessible hole (diameter ~ 10 Å) exposing directly the external face of helix α2 right behind A426-A427 (Figure 6A). The 3_{-10} helix and the stiff U-turn structures are lost resulting in a drastic reorientation of R361-R362-Q367, which contrary to the native conformation, point in opposite directions (Figure 6B). The Y364 phenol ring no longer occupies the center of the cavity and instead points toward the solvent displaying two different conformations. Residue R440, serving as the last link in the hydrophobic network, moves drastically away from the NTE. A slight conformational change of the first helix α2 turn disturbs the conformation of some lateral chains, placed just upstream on the canonical structure (Figure S2B). The cooperative nature of this hydrophobic network was further validated by all atoms molecular dynamic simulations. These show that conformational instability and large fluctuation of both NTE and CTE are observed in the absence of F359 (Figure S3).

The relevance of such conformational rearrangements was further investigated in solution under protein concentrations that ensure compactness of the mutant's protein matrix. Mild-proteolysis using trypsin coupled to LC-MS analysis identify cleavages of F359A and Y364A mutants but not of the wild type protein, at a site just after R362 indicating a flexible NTE and show that this site is protected from cleavage by tRNA binding (Figure S4). The mutants display a comparable radius of gyration determined by SAXS, which is slightly larger than that of the wild type protein by ~ 2 Å (Figure S5E). Their normalized Kratky plot is consistent with a more dynamic nature and less globular/compact protein matrix (Figure S5A). In addition, the theoretical SAXS curve obtained from F359A crystal structure fits well the experimental X-ray diffusion curve of both mutants (Figure S5B-D). The structural changes were further corroborated at single-residue level by NMR. The (^{1}H,^{15}N) correlation spectra of the two mutants present resonances broadening effects indicating that both mutations introduce one or more dynamic processes that are not observed in the wild type protein (Figure S6). Moreover, chemical shifts changes confirmed that the NTE, the N-terminal tip of helix α2

as well as the CTE are the dsRBD regions most affected by the mutations (Figure S7). Therefore, F359A mutant crystal structure is a relevant form in solution and Y364A protein may share a closely related structure.

Discussion

In contrast to the vast majority of the dihydrouridine synthases(*18-22*), we have recently shown that hDus2 (and more generally animal Dus2), which catalyzes D20 synthesis in tRNA, uses for substrate recognition an extended dsRBD carrying both NTE and CTE(*17*). Specifically, the NTE plays a key role in the adaptation of this domain to tRNA recognition by providing three important residues to interact with the T-arm of the tRNA, namely R361, R362 and Q367(*15*). Here we pushed further the investigation on this NTE by unequivocally establishing its critical role to the folding and thermodynamic stability of the overall dsRBD.

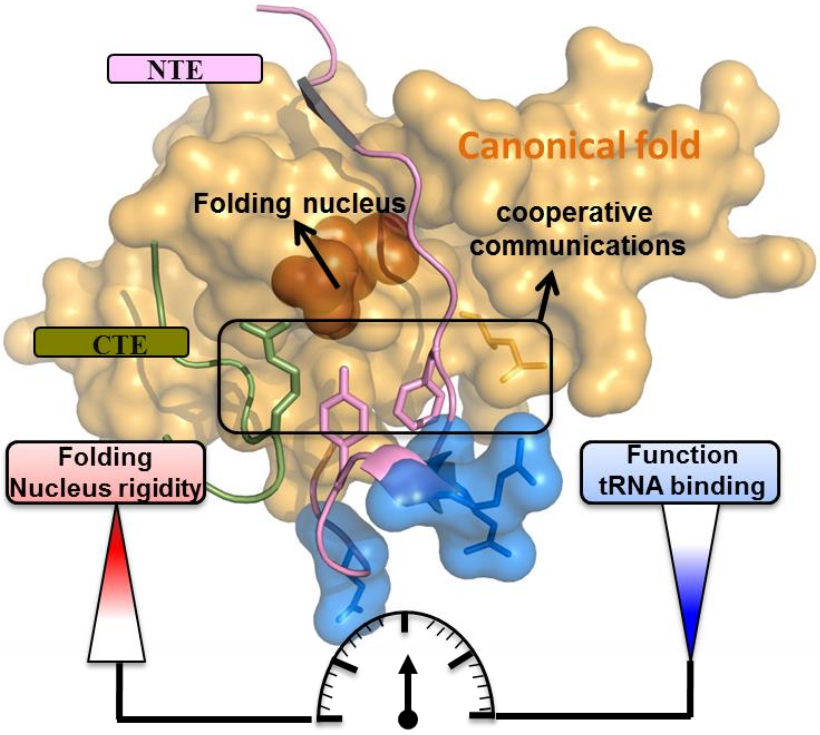

Figure 7 Molecular mechanisms for the adaptation of a dsRBD to tRNA binding function. The scheme shows how NTE and CTE of hDus2 dsRBD act as allosteric effectors, specifically via implementation of a hydrophobic and cooperative long range network, to couple novel function (via R361 and R362 brought by NTE and involved in tRNA recognition) and thermodynamic stabilization of the evolved system by the increase of the folding nucleus (A426-A427) rigidity of an otherwise intrinsically unstable canonical dsRBD fold. This lead us to propose that (i) intrinsic flexibility of a canonical fold could promote its evolvability and (ii) cooperative communication is a determinant factor in ensuring a thermodynamic viability to the evolved system.

This is made possible by the implementation of a hydrophobic network involving residues L421 from the N-terminal tip of helix α2, F359 and Y364 from the NTE and R440 (aliphatic side chain) from the CTE (Figure 7). This network lies in front of helix α2 thus extending further the hydrophobic core of the domain, and in the immediate vicinity of R361, R362 and Q367, which specialize the dsRBD for tRNA recognition. We showed that F359 and Y364 residues enable a communicative and cooperative link between the NTE, CTE and hydrophobic core of the canonical fold via A426 and A427, two residues located in the inner face of helix α2 (Figure 7). Indeed, deletion of NTE or mutation of F359 or Y364 converts dsRBD into an extremely flexible and inherently unstable protein that unfolds irreversibly. Our structural and computational data provide a satisfactory explanation of the mechanism of action of these extensions. The NTE and CTE create a hydrophobic chamber that envelops the external face of helix α2. This hydrophobic network (i) strengthens the hydrophobic core of the canonical fold by protecting the latter from competitive and destabilizing interactions with the solvent, and (ii) structures the helix 3-10 carrying R361-R362 and the U-turn containing Q367, residues involved in the recognition of tRNA (Figure 7). This ensures a stable thermodynamic folding of hDus2-dsRBD while selecting the functional conformation adapted for tRNA recognition. Presumably, the implementation of a hydrophobic network allowing a cooperative communication between the canonical fold and its extension(s) could be one of the critical features by which the dsRBD adapts to new functions. Besides hDus2, other extended dsRBDs tend to support this proposition such as the case of *Saccharomyces cerevisiae* RNase III enzyme Rnt1p or *Schizosaccharomyces pombe* Dicer Dcr1. In Rnt1p, the presence of an extended hydrophobic core between the canonical α1–β1 loop and the extension (helix α3) stabilizes the canonical structure and acts as a dynamic hinge that allows a concerted change in the positions of helix α1 between the free and RNA bound states, a key feature of substrate recognition by the Rnt1p dsRBD(*16*). Similarly, in Dcr1 dsRBD a hydrophobic network observed between a C-terminal extension embedding a zinc-binding site and the canonical structure stabilizes the overall structure and the control of Dcr1 subcellular localization(*12*).

Importantly, it seems that different stabilization strategies of the peculiar canonical structure of the dsRBD were selected during the evolution. For most of the dsRBDs studied so far, the hydrophobic core of the canonical fold appears self-sufficient to promote a stable structure. Indeed, dsRBDs conserve several hydrophobic residues in helix α1, α2 and strands β1 and β2 that stabilize the canonical structure (*8*). Even though reported only with the ribonuclease DCL1 from *Arabidopsis thaliana*, the second possibility is a dsRBD existing under an intrinsically disordered state for which the RNA itself plays the role of structuring agent by a conventional ligand binding induced-folding mechanism (*52-54*). Specifically, helix α2 of DCL1 dsRBD is proposed to serve as a nucleation site for the folding event triggered by the RNA substrate. The third and last mechanism is the one concerning hDus2 dsRBD and more broadly extended dsRBDs. These dsRBD may also exhibit an intrinsically unstable canonical fold, but in those specific cases, the extensions themselves act as folding effectors or a hydrophobic clamp by strengthening the nucleation site(s) of the canonical fold in *trans*. In essence, the present work concurs to support the concept that *trans* and long-range hydrophobic interactions are dominant factors in the cooperativity of protein folding and constitute the major driving force in polypeptide collapse leading to stable and functional native states (*55-58*).

Associated content

Supporting information

Table S1: Summary of data collection and refinement statistics.

Table S2: Thermodynamic and kinetics parameters characterizing dsRDB stability, determined by urea-induced denaturation experiments.

Figure S1: Rigidity profiles for all the dsRBDs in the multiple sequence alignment.

Figure S2: Structural comparison of wild type hDus2-dsRDB with its F359A mutant.

Figure S3: Conformational characterization of wild type and F359A dsRDBs by molecular dynamic.

Figure S4: Structural characterization of dsRBD wild type, F359A and Y364A mutants.

Figure S5: SAXS characterization of dsRBD and its F359A and Y364A dRBD mutants.

Figure S6: NMR spectra of the dsRBDs showing line broadening for certain residues in the mutants F359A and Y364A.

Figure S7: Chemical shift changes in F359A and Y364A dsRBD mutants.

Accession Codes

PDB: 6EI8

Author information

Corresponding Author

*Email : djemel.hamdane@college-de-france.fr. Telephone : +33-(0)1-44271645.

Notes

The authors declare no competing financial interest.

Acknowledgements

This work was supported by the Centre National de la Recherche Scientifique, université Pierre et Marie Curie as well as program from the French State (ANR-15-CE11-0004-01 and Grant“DYNAMO”, ANR-11-LABX-0011-01). We also acknowledge SOLEIL for provision of synchrotron radiation facilities (proposal ID 20150780) and we would like to thank Proxima 2 for assistance in using the beamline.

References

1. Anantharaman, V., Koonin, E. V., and Aravind, L. (2002) Comparative genomics and evolution of proteins involved in RNA metabolism, *Nucleic Acids Res 30*, 1427-1464.
2. Bycroft, M., Grunert, S., Murzin, A. G., Proctor, M., and St Johnston, D. (1995) NMR solution structure of a dsRNA binding domain from Drosophila staufen protein reveals homology to the N-terminal domain of ribosomal protein S5, *EMBO J 14*, 3563-3571.
3. Saunders, L. R., and Barber, G. N. (2003) The dsRNA binding protein family: critical roles, diverse cellular functions, *FASEB J 17*, 961-983.

4. Tian, B., Bevilacqua, P. C., Diegelman-Parente, A., and Mathews, M. B. (2004) The double-stranded-RNA-binding motif: interference and much more, *Nat Rev Mol Cell Biol 5*, 1013-1023.
5. Chang, K. Y., and Ramos, A. (2005) The double-stranded RNA-binding motif, a versatile macromolecular docking platform, *FEBS J 272*, 2109-2117.
6. Kharrat, A., Macias, M. J., Gibson, T. J., Nilges, M., and Pastore, A. (1995) Structure of the dsRNA binding domain of E. coli RNase III, *EMBO J 14*, 3572-3584.
7. Ryter, J. M., and Schultz, S. C. (1998) Molecular basis of double-stranded RNA-protein interactions: structure of a dsRNA-binding domain complexed with dsRNA, *EMBO J 17*, 7505-7513.
8. Masliah, G., Barraud, P., and Allain, F. H. (2013) RNA recognition by double-stranded RNA binding domains: a matter of shape and sequence, *Cell Mol Life Sci 70*, 1875-1895.
9. Gleghorn, M. L., and Maquat, L. E. (2014) 'Black sheep' that don't leave the double-stranded RNA-binding domain fold, *Trends Biochem Sci 39*, 328-340.
10. Leulliot, N., Quevillon-Cheruel, S., Graille, M., van Tilbeurgh, H., Leeper, T. C., Godin, K. S., Edwards, T. E., Sigurdsson, S. T., Rozenkrants, N., Nagel, R. J., Ares, M., and Varani, G. (2004) A new alpha-helical extension promotes RNA binding by the dsRBD of Rnt1p RNAse III, *EMBO J 23*, 2468-2477.
11. Wu, H., Henras, A., Chanfreau, G., and Feigon, J. (2004) Structural basis for recognition of the AGNN tetraloop RNA fold by the double-stranded RNA-binding domain of Rnt1p RNase III, *Proc Natl Acad Sci U S A 101*, 8307-8312.
12. Barraud, P., Emmerth, S., Shimada, Y., Hotz, H. R., Allain, F. H., and Buhler, M. (2011) An extended dsRBD with a novel zinc-binding motif mediates nuclear retention of fission yeast Dicer, *EMBO J 30*, 4223-4235.
13. Barraud, P., Banerjee, S., Mohamed, W. I., Jantsch, M. F., and Allain, F. H. (2014) A bimodular nuclear localization signal assembled via an extended double-stranded RNA-binding domain acts as an RNA-sensing signal for transportin 1, *Proc Natl Acad Sci U S A 111*, E1852-1861.
14. Banerjee, S., and Barraud, P. (2014) Functions of double-stranded RNA-binding domains in nucleocytoplasmic transport, *RNA Biol 11*, 1226-1232.
15. Bou-Nader, C., Barraud, P., Pecqueur, L., Perez, J., Velours, C., Shepard, W., Fontecave, M., Tisne, C., and Hamdane, D. (2019) Molecular basis for transfer RNA recognition by the double-stranded RNA-binding domain of human dihydrouridine synthase 2, *Nucleic Acids Res 47*, 3117-3126.
16. Hartman, E., Wang, Z., Zhang, Q., Roy, K., Chanfreau, G., and Feigon, J. (2013) Intrinsic dynamics of an extended hydrophobic core in the S. cerevisiae RNase III dsRBD contributes to recognition of specific RNA binding sites, *J Mol Biol 425*, 546-562.
17. Bou-Nader, C., Pecqueur, L., Bregeon, D., Kamah, A., Guerineau, V., Golinelli-Pimpaneau, B., Guimaraes, B. G., Fontecave, M., and Hamdane, D. (2015) An extended dsRBD is required for post-transcriptional modification in human tRNAs, *Nucleic Acids Res 43*, 9446-9456.
18. Yu, F., Tanaka, Y., Yamashita, K., Suzuki, T., Nakamura, A., Hirano, N., Yao, M., and Tanaka, I. (2011) Molecular basis of dihydrouridine formation on tRNA, *Proc Natl Acad Sci U S A 108*, 19593-19598.
19. Byrne, R. T., Jenkins, H. T., Peters, D. T., Whelan, F., Stowell, J., Aziz, N., Kasatsky, P., Rodnina, M. V., Koonin, E. V., Konevega, A. L., and Antson, A. A. (2015) Major reorientation of tRNA substrates defines specificity of dihydrouridine synthases, *Proc Natl Acad Sci U S A 112*, 6033-6037.
20. Bou-Nader, C., Montemont, H., Guerineau, V., Jean-Jean, O., Bregeon, D., and Hamdane, D. (2018) Unveiling structural and functional divergences of bacterial tRNA dihydrouridine synthases: perspectives on the evolution scenario, *Nucleic Acids Res 46*, 1386-1394.
21. Lombard, M., and Hamdane, D. (2017) Flavin-dependent epitranscriptomic world, *Arch Biochem Biophys 632*, 28-40.

22. Bou-Nader, C., Bregeon, D., Pecqueur, L., Fontecave, M., and Hamdane, D. (2018) Electrostatic Potential in the tRNA Binding Evolution of Dihydrouridine Synthases, *Biochemistry 57*, 5407-5414.
23. Henzler-Wildman, K., and Kern, D. (2007) Dynamic personalities of proteins, *Nature 450*, 964-972.
24. Boehr, D. D., Nussinov, R., and Wright, P. E. (2009) The role of dynamic conformational ensembles in biomolecular recognition, *Nat Chem Biol 5*, 789-796.
25. Maria-Solano, M. A., Serrano-Hervas, E., Romero-Rivera, A., Iglesias-Fernandez, J., and Osuna, S. (2018) Role of conformational dynamics in the evolution of novel enzyme function, *Chem Commun (Camb) 54*, 6622-6634.
26. Tisne, C., Rigourd, M., Marquet, R., Ehresmann, C., and Dardel, F. (2000) NMR and biochemical characterization of recombinant human tRNA(Lys)3 expressed in Escherichia coli: identification of posttranscriptional nucleotide modifications required for efficient initiation of HIV-1 reverse transcription, *RNA 6*, 1403-1412.
27. Chou, F. C., Sripakdeevong, P., Dibrov, S. M., Hermann, T., and Das, R. (2013) Correcting pervasive errors in RNA crystallography through enumerative structure prediction, *Nat Methods 10*, 74-76.
28. Vonrhein, C., Flensburg, C., Keller, P., Sharff, A., Smart, O., Paciorek, W., Womack, T., and Bricogne, G. (2011) Data processing and analysis with the autoPROC toolbox, *Acta Crystallogr D Biol Crystallogr 67*, 293-302.
29. Lavery, R., and Sacquin-Mora, S. (2007) Protein mechanics: a route from structure to function, *Journal of Biosciences 32*, 891-898.
30. Sacquin-Mora, S. (2014) Motions and mechanics: investigating conformational transitions in multi-domain proteins with coarse-grain simulations, *Mol. Simul. 40*, 229-236.
31. Sacquin-Mora, S. (2016) Bridging Enzymatic Structure Function via Mechanics: A Coarse-Grain Approach, *Methods in Enzymology 578*, 227-248.
32. Yang, S. W., Chen, H. Y., Yang, J., Machida, S., Chua, N. H., and Yuan, Y. A. (2010) Structure of Arabidopsis HYPONASTIC LEAVES1 and its molecular implications for miRNA processing, *Structure 18*, 594-605.
33. Barraud, P., Heale, B. S., O'Connell, M. A., and Allain, F. H. (2012) Solution structure of the N-terminal dsRBD of Drosophila ADAR and interaction studies with RNA, *Biochimie 94*, 1499-1509.
34. Gan, J., Shaw, G., Tropea, J. E., Waugh, D. S., Court, D. L., and Ji, X. (2008) A stepwise model for double-stranded RNA processing by ribonuclease III, *Mol Microbiol 67*, 143-154.
35. Zacharias, M. (2003) Protein-protein docking with a reduced protein model accounting for side-chain flexibility, *Protein Sci 12*, 1271-1282.
36. Tozzini, V. (2005) Coarse-grained models for proteins, *Curr Opin Struct Biol 15*, 144-150.
37. Ermak, D. L., and McCammon, J. A. (1978) Brownian dynamics with hydrodynamic interactions, *J. Chem. Phys. 69*, 1352-1360.
38. Pastor, R. W., Venable, R., and Karplus, M. (1988) Brownian dynamics simulation of a lipid chain in a membrane bilayer, *J Chem Phys 89*, 1112-1127.
39. Papadopoulos, J. S., and Agarwala, R. (2007) COBALT: constraint-based alignment tool for multiple protein sequences, *Bioinformatics 23*, 1073-1079.
40. Kaminski, G. A., Friesner, R. A., Tirado-Rives, J., and Jorgensen, W. L. (2001) Evaluation and reparametrization of the OPLS-AA force field for proteins via comparison with accurate quantum chemical calculations on peptides, *J. Phys. Chem. B 105*, 6474-6487.
41. Jorgensen, W. L., Chandrasekhar, J., Madura, J. D., Impey, R. W., and Klein, M. L. (1983) Comparison of Simple Potential Functions for Simulating Liquid Water, *Journal of Chemical Physics 79*, 926-935.
42. Bussi, G., Donadio, D., and Parrinello, M. (2007) Canonical sampling through velocity rescaling, *Journal of Chemical Physics 126*, 014101.
43. Hess, B., Bekker, H., Berendsen, H. J. C., and Fraaije, J. (1997) LINCS: A linear constraint solver for molecular simulations, *J. Comp. Chem. 18*, 1463-1472.
44. Essmann, U., Perera, L., Berkowitz, M. L., Darden, T., Lee, H., and Pedersen, L. G. (1995) A SMOOTH PARTICLE MESH EWALD METHOD, *J. Chem. Phys. 103*, 8577-8593.

45. Parrinello, M., and Rahman, A. (1981) Polymorphic transitions in single crystals: A new molecular dynamics method, *Journal of Applied Physics 52*, 7182-7190.
46. Sacquin-Mora, S. (2015) Fold and flexibility: what can proteins' mechanical properties tell us about their folding nucleus?, *J R Soc Interface 12*.
47. Sacquin-Mora, S. (2016) Bridging Enzymatic Structure Function via Mechanics: A Coarse-Grain Approach, *Methods Enzymol 578*, 227-248.
48. Bocahut, A., Bernad, S., Sebban, P., and Sacquin-Mora, S. (2011) Frontier residues lining globin internal cavities present specific mechanical properties, *J Am Chem Soc 133*, 8753-8761.
49. Theillet, F. X., Binolfi, A., Frembgen-Kesner, T., Hingorani, K., Sarkar, M., Kyne, C., Li, C., Crowley, P. B., Gierasch, L., Pielak, G. J., Elcock, A. H., Gershenson, A., and Selenko, P. (2014) Physicochemical properties of cells and their effects on intrinsically disordered proteins (IDPs), *Chem Rev 114*, 6661-6714.
50. Politou, A., and Temussi, P. A. (2015) Revisiting a dogma: the effect of volume exclusion in molecular crowding, *Curr Opin Struct Biol 30*, 1-6.
51. Hamdane, D., Velours, C., Cornu, D., Nicaise, M., Lombard, M., and Fontecave, M. (2016) A chemical chaperone induces inhomogeneous conformational changes in flexible proteins, *Phys Chem Chem Phys 18*, 20410-20421.
52. Suarez, I. P., Burdisso, P., Benoit, M. P., Boisbouvier, J., and Rasia, R. M. (2015) Induced folding in RNA recognition by Arabidopsis thaliana DCL1, *Nucleic Acids Res 43*, 6607-6619.
53. Suarez, I. P., Gauto, D. F., Hails, G., Mascali, F. C., Crespo, R., Zhao, L., Wang, J., and Rasia, R. M. (2018) Conformational sampling of the intrinsically disordered dsRBD-1 domain from Arabidopsis thaliana DCL1, *Phys Chem Chem Phys 20*, 11237-11246.
54. Wright, P. E., and Dyson, H. J. (2009) Linking folding and binding, *Curr Opin Struct Biol 19*, 31-38.
55. Han, J. H., Batey, S., Nickson, A. A., Teichmann, S. A., and Clarke, J. (2007) The folding and evolution of multidomain proteins, *Nat Rev Mol Cell Biol 8*, 319-330.
56. Parbhoo, N., Stoychev, S. H., Fanucchi, S., Achilonu, I., Adamson, R. J., Fernandes, M., Gildenhuys, S., and Dirr, H. W. (2011) A conserved interdomain interaction is a determinant of folding cooperativity in the GST fold, *Biochemistry 50*, 7067-7075.
57. Aksel, T., Majumdar, A., and Barrick, D. (2011) The contribution of entropy, enthalpy, and hydrophobic desolvation to cooperativity in repeat-protein folding, *Structure 19*, 349-360.
58. Chandler, D. (2005) Interfaces and the driving force of hydrophobic assembly, *Nature 437*, 640-647.

For Table of contents use only:

Conformational stability adaptation of a double-stranded RNA binding domain to transfer RNA ligand

Charles Bou-Nader, Ludovic Pecqueur, Pierre Barraud, Marc Fontecave, Carine Tisné, Sophie Sacquin-Mora, and Djemel Hamdane

TOC

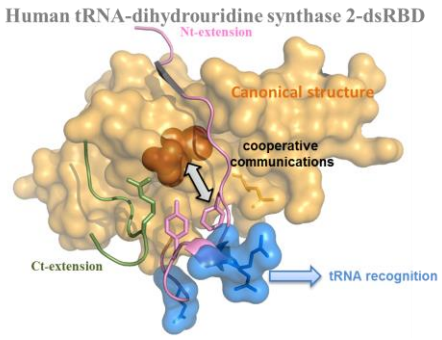
Human tRNA-dihydrouridine synthase 2-dsRBD
Nt-extension
Canonical structure
cooperative
communications
Ct-extension
tRNA recognition